# Forward Flight Study of a Power-efficient Disc-shaped UAV: a Computational Approach

Samia Shahrin Ahmed Snikdha[1], Shih-Hsiung Chen[1]

1. Department of Aeronautics & Astronautics, National Cheng Kung University, No. 1 University Rd, Tainan 70101, Taiwan (R.O.C.).

**Abstract**

This study investigates a disc-shaped unmanned aerial vehicle (UAV) engineered with a contoured upper surface to improve forward-flight efficiency. A three-dimensional CFD model, validated through mesh-sensitivity analysis, is used to quantify aerodynamic performance across forward speeds of 25–100 km/h and varying rotor and tilt configurations. The curved body generates up to 80.5% of total lift in level flight, reducing power demand by as much as 66.42% relative to hover. Maximum efficiency occurs at small negative angles of attack, where body inclination and surface geometry enhance the lift-to-drag ratio. Power savings increase from 48.31% at 25 km/h to 80.26% at 100 km/h. These results demonstrate how geometric shaping and attitude control can be leveraged to improve the aerodynamic and energy performance of non-conventional UAV platforms.

**Keywords**: Aerodynamics, Computational fluid dynamics (CFD), Disc-shaped UAV, Drone, Straight and level flight, Power.

## 1. Introduction

Unmanned aerial vehicles (UAVs) are increasingly used in civilian and industrial applications such as precision agriculture, infrastructure inspection, search-and-rescue, and remote sensing, driving the need for longer endurance and improved energy efficiency. Although multirotor UAVs dominate VTOL operations due to their simplicity and maneuverability, their reliance on rotor-generated lift results in high power consumption and limited range [1], [2], [3]. Prior efforts to enhance efficiency through shrouded rotors, curved bodies, or auxiliary lifting surfaces have shown potential [4], [5], [6], [7] yet many designs either require high-power propulsion systems, lose effectiveness at higher forward speeds, or provide only modest gains in endurance [8], [9], [10], [11].

Forward-flight aerodynamics of non-conventional UAV geometries remain insufficiently characterized, as most existing studies focus on hovering conditions. Recent measurements show that thrust, power, and noise increase significantly with freestream velocity in standard quadcopters [12], [13], underscoring the need for airframe designs that reduce rotor loading.. The ducted rotor associated with a disc-shaped body having the curvature effect offers some distinct advantages over the standard multirotor UAVs due to their robust frame design providing crash resistance, flight safety, and power-efficient aerodynamic performance. Disc-shaped and ducted-rotor configurations offer structural robustness and safety advantages, [14] but their

aerodynamic behavior in forward flight has not been comprehensively analyzed. Existing power-estimation approaches—such as hybrid blade-element momentum models, endurance-based methods, and drag-weight analyses—do not fully capture the coupled effects of body lift, rotor loading, and vehicle attitude in such geometries [15], [16], [17].

This study investigates the forward-flight aerodynamics of a disc-shaped VTOL UAV with a convex upper surface and ducted rotor, designed to exploit body-generated lift to reduce rotor power demand. Three-dimensional CFD simulations are used to quantify how forward speed, tilt angle, and rotor speed influence lift, drag, and power consumption. CFD provides a practical and reliable means to analyze complex flow structures prior to experimental testing and is widely used in aerospace design [18], [19].

To the best of our knowledge, our study presents a new idea, which aims to generate substantial lift from the UAV body, lessening the load on the rotor. This leads to a greater percentage of power saved and emerges an idea of economic drone flight. The study integrates a range of flight conditions considering a strategy to start transition to forward flight from a negative angle of attack. In this context, the main objective of designing the disc-shaped UAV body is to obtain a substantial contribution of lift while sustaining the vehicle weight in straight and level flight that will affect in decreasing the power consumption by the rotor. To this end, we address CFD-based research on the optimal aerodynamic performance of the disc-shaped UAV configuration in forward flight with specific focus on the maximum lift-to-drag ratio with minimum power consumption of the rotor during inclined vehicle attitudes. The purpose here is to obtain the precise behavior of the UAV with rotor, rather than investigating the subtle behavior of each blade.

## 2. Geometry Design: The disc-shaped UAV

Different profiles of the disc-shaped VTOL UAV are presented in Figure 1 by the application of the engineering design software *Solidworks2018*. For an adequate lift-to-drag ratio we designed the rotor blades considering the NACA 4424 airfoil profile with maximum thickness at the position of 24% of the chord from the leading edge. Figure 2 depicts views of the blade configuration integrated to the rotor.

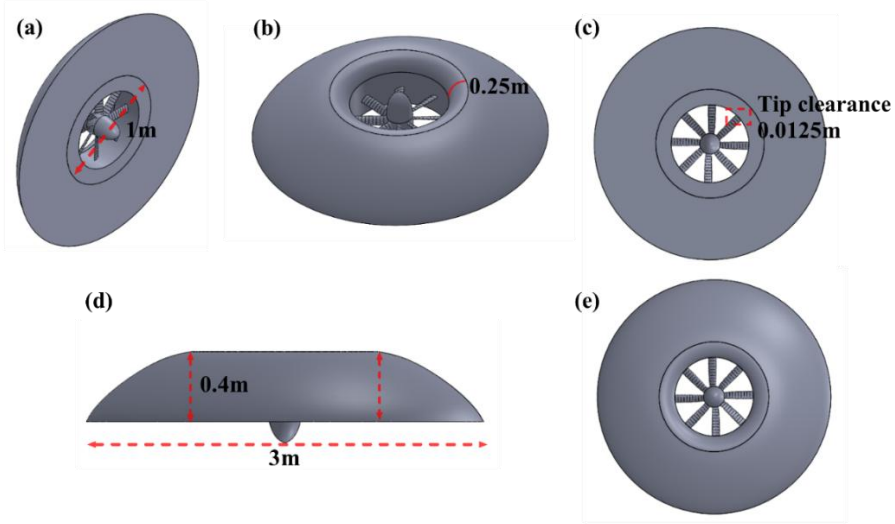

Figure 1: 3-D views with design parameters of the disc-shaped UAV. (a) isometric view, (b) upside-down view, (c) bottom view, (d) side view, and (e) top view.

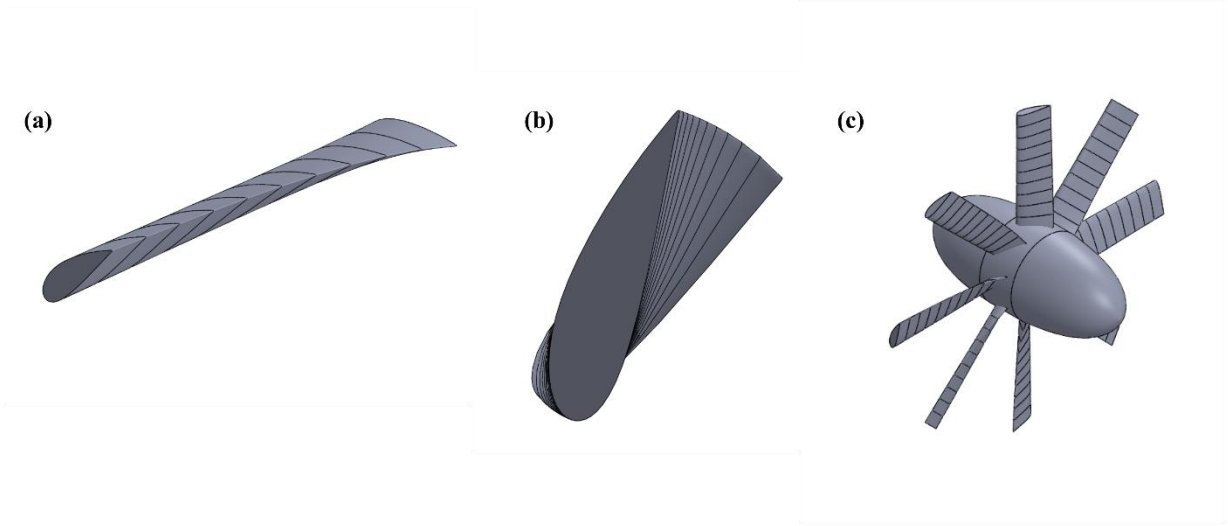


Figure 2: Blade views integrated into the rotor. (a) isometric view, (b) front view displaying the stagger angles, (c) eight lofted blades attached to the hub of the rotor (isometric view).

The aerodynamic center is at 25mm which is one-fourth of the optimized chord length. The rotor consists of eight blades, each with flow inlet angles (β) varying from $48.34^o - 77.46^o$. As a general rule, with the increase in the number of blades the mass flow rate increases; however, the flow rate tends to remain unaltered for a rotor with more than five blades [20]. Table 1 explains the geometry parameters in detail. A disc-shaped body with an upper surface curvature was designed adjoining the central rotor. The UAV is designed to accommodate the transition from hover to the forward flight phase at low RPM of the spinning rotor with substantial lift contribution from the body upper surface. A preliminary study of Nigel Q. Kelly et al. [21] ranged the orifice to the radius of curvature as $0.35 < \frac{h_o}{R_c} < 0.25$, however, the design caused a significant rise of high pressure near the orifice leading to a reduced thrust. As a result, to achieve the maximum thrust we optimized the design with a larger $h_o/R_c$ ratio of 1.6 with $h_o = 0.4$m and $R_c = 0.25$m. A large upper body curvature enhances the UAV performance with prolonged flow entrainment speeding up in the forward flight. The outer diameter of the body is set to be $3m$ and the weight is measured to be $1090$N, obtained by considering the net hover thrust from our previous study [4]. The central rotor increases the velocity of air circulation around the wing-like body. This air circulation around the body in return generates lift on the UAV, according to the lifting theory of curvature bodies. Moreover, an additional lift is produced as soon as the flow gets entrained by the curved upper surface of the drone body in the cruise flight. The forward flight speed of the vehicle was tested in the range of $25 - 100$ km/h with the effect of inclinations. Figure 3 explains the planar view of the UAV in straight and level flight where the vehicle is slightly inclined to the direction of motion. The lifting body plays the role of a wing and provides extra lift during forward flight. We configured this shape of the UAV body aiming to reduce the load on the rotor with supporting lift from the body during forward flight.

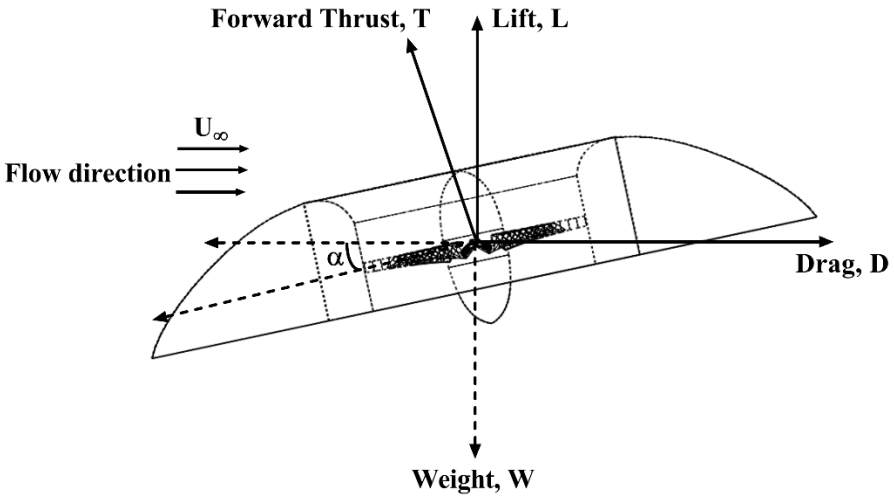


Figure 3: Schematics of the aerodynamic forces acting on the UAV with tilt angle, α in straight and level flight.

Table 1: Design Parameters.

| UAV Parts | Parameter (m) |
|---|---|
| Body Diameter | 3 |
| Duct height | 0.4 |
| Duct lip arc radius | 0.25 |
| Hub diameter | 0.135 |
| Tip clearance | 0.0125 |
| Rotor Diameter | 1 |

## 3. Materials and Methods

*3.1 Numerical Assumptions*

*3.1.1 Lift and Thrust equations*

Straight and level flight of the UAV is simulated while maintaining the vehicle weight at a range of forward speeds of $25 - 100$ km/h. When the UAV is maneuvering in straight and level flight mode, all aerodynamic forces should be balanced at a constant altitude. The forward thrust, T produced by the rotor opposes the retarding drag force, D parallel to the relative wind.

$$T = D \tag{3.1}$$

While flying at a constant altitude, the state of quasi-equilibrium is obtained by adjusting lift, L to match the UAV's weight, W.

$$L = W \tag{3.2}$$

$$\frac{L}{D} = \frac{W}{T} \tag{3.3}$$

The ratio of the lift force to the drag force, $L/D$ gives the measure of the UAV design efficiency. Similarly, thrust can also be expressed as a function of weight in terms of $L/D$ to give a measure of the UAV efficiency. From equation (3.1) and (3.2) we have, $T = \frac{D}{L}W$ or, $T = \frac{1}{\frac{L}{D}}W$. Since weight of the UAV is constant, thrust is proved to be inversely proportional to $L/D$. Thus, the higher the lift-to-drag ratio, the less the forward thrust and the higher the UAV efficiency. In order to sustain the weight, the lift steadiness of the UAV is obtained by adjusting the rotor RPM. In the proposed design, the disc-shaped UAV body with the upper surface curvature is conceptualized to obtain a significant decrease in rotor RPM required while maintaining the forward level flight. With each rotation per second of the rotor blades, the work done on the UAV is equal to the gain in energy of the fluid per unit time or the power consumed by the rotor.

*3.1.2 Rotor power requirements in forward flight*

The rotor power in forward flight is given by the equation, $P = T(V_\infty \sin\alpha + v_i)$ (3.4)

Where, $TV_\infty \sin\alpha$ is the power required to propel the rotor forward, $Tv_i$ is the induced power, and $\alpha$ is the disc angle of attack. For horizontal equilibrium, $T\sin\alpha = D\cos\alpha \approx D$. Therefore, $\tan\alpha = \frac{D}{W} = \frac{D}{L} \approx \frac{D}{T}$ which is expressed in terms of the UAV's lift-to-drag ratio. The lift during the inclined flight is divided into two components- the vertical force called the 'lift' and the forward force called the 'thrust'. In order to generate forward thrust, quadcopters like helicopters need to lean towards the flight path with negative angle of attack ($AOA < 0$). With a negative AOA, the rotor disc plane bends from the rotation axis generating a forward thrust to share the lift by balancing the vehicle weight.

*3.1.3 Drag calculation in forward flight*

The air resistance or the drag force, D acting on the aircraft in the opposite direction of motion is given by the equation, $D = \frac{1}{2}C_D\rho V^2 A$ (3.5)

Where $C_D$ is the drag coefficient that depends on the shape of the UAV, $\rho$ (kg/m$^3$) is the air density, $V$ (m/s) is the forward speed relative to the surrounding air, and $A$ (m$^2$) is the cross-sectional area of the UAV moving through the air. During forward flight, the UAV is angled in the direction of motion providing an equal and opposite force to the drag. Thus, the tilt mechanism has a forward component to balance the reaction force the air exerts on the UAV. Meanwhile, the UAV body surfaces share the lift to compensate for the loss of altitude.

*3.2 Computational Modeling*

High-fidelity computational fluid dynamics simulations (CFD) were performed using the widely used [22], [23], [24] ANSYS CFX flow simulation software. The set of governing equations solved by ANSYS CFX is the unsteady Navier Stokes (NS) equations in their conservative form as follows.

The continuity equation: $\frac{\partial \rho}{\partial t} + \nabla.(\rho U) = 0$ (3.6)

The momentum equation: $\frac{\partial (\rho U)}{\partial t} + \nabla.(\rho U \otimes U) = -\nabla p + \nabla.\tau + S_M$ (3.7)

Where the stress tensor, τ is related to the strain rate by, $\tau = \mu(\nabla U + (\nabla U)^T - \frac{2}{3}\delta \nabla.U)$.

The total energy equation: $\frac{\partial \rho h_{tot}}{\partial t} - \frac{\partial p}{\partial t} + \nabla.(\rho U h_{tot}) = \nabla(\lambda \nabla T) + \nabla.(U.\tau) + U.S_M + S_E$(3.8)

Where $h_{tot}$ is the total enthalpy, related to the static enthalpy by, $h_{tot} = h_{stat} + \frac{1}{2}U^2$ (3.9)

The term, $\nabla.(U.\tau)$ is the viscous work term, and $U.S_M$ represents the work due to external momentum sources and is currently ignored. This paper uses the total energy model where the ANSYS CFX solver directly computes the total enthalpy and derives the static enthalpy from the equation (3.9). For flows in the rotating frame of reference, additional sources of momentum are included to account for the effect of the Coriolis force and the centrifugal force.

$S_M = S_{cor} + S_{cfg}$, where, $S_{cor} = -2\rho\omega \times U$ and $S_{cfg} = -\rho\omega \times (\omega \times r)$, where $r$ is the location vector and $U$ is the rotating frame velocity. In the energy equation of the rotating domain, the advection of the total enthalpy is replaced by the advection of the rothalpy, $I$ given by, $I = h_{stat} + \frac{1}{2}U^2 - \frac{1}{2}\omega^2 R^2$. In principle, the NS equations describe both laminar and turbulent flows, however, at realistic Reynolds numbers of turbulent flows a large span of turbulent length and time scales by the use of turbulence models are applied. With a modification of the original unsteady NS equations, these models involve an additional time-varying fluctuating component to produce the Reynolds Averaged Navier Stokes (RANS) equations given in equation (3.10-3.12). Simulation of the RANS equation greatly reduces the computational effort compared to a direct numerical simulation and is generally adopted for practical engineering calculations.

$\frac{\partial \rho}{\partial t} + \nabla.(\rho U) = 0$ (3.10)

$\frac{\partial \rho U}{\partial t} + \nabla.\{\rho U \otimes U\} = \nabla.\{\tau - \rho\overline{u \otimes u}\} + S_M$ (3.11)

The continuity equation has remained unaltered. However, the momentum and scalar transport equations now contain turbulent flux terms additional to the molecular diffusive fluxes. These are the Reynolds stress, $\rho\overline{u \otimes u}$ and the Reynolds flux, $\rho\overline{u\Phi}$. They reflect the fact that convective transport due to turbulent velocity fluctuations acts to enhance mixing over and above that caused by thermal fluctuations of the air.

The Reynolds averaged energy equation:

$\frac{\partial \rho h_{tot}}{\partial t} - \frac{\partial p}{\partial t} + \nabla.(\rho U h_{tot}) = \nabla.(\lambda \nabla \tau - \rho\overline{uh}) + \nabla.(U.\tau) + S_E$. (3.12)

Turbulence models bring closure to the RANS equations by applying models for the computation of the Reynolds stress and Reynolds fluxes. This study uses one of the many eddy viscosity turbulence models, namely $k - \omega$ based $SST$ model that accounts for the transport of the turbulent

shear stress and gives highly accurate predictions of the amount of flow separations under adverse pressure gradients. The $k-\omega$ based $SST$ model formulates the eddy viscosity with a limiter as, $\upsilon_t = \frac{a_1 k}{\max(a_1\omega, SF_2)}$ where, $\upsilon_t = \frac{\mu_t}{\rho}$ and $F_2$ is a blending function that restricts the limiter to the wall boundary layer. In order to resolve the region in close proximity to the laminar and transitional boundary layers, the turbulence equations used the high-resolution discretization scheme, a bounded second order upwind biased discretization.

*3.3 Computational Mesh*

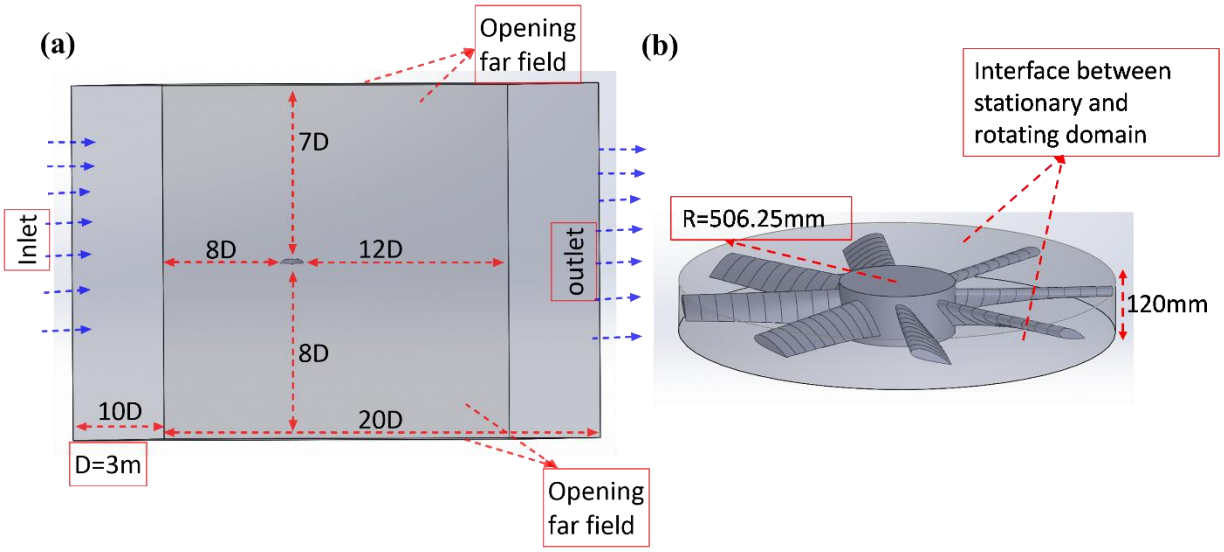


Figure 4: Computational domain. (a) Rectangular parallelopiped stationary domain and (b) cylindrical rotating domain.

Figure 4 describes the computational domains applied for the forward flight simulations. A sufficiently large rectangular domain of dimension $20D \times 10D \times 15D$ was considered for the computations, where $D$ stands for the UAV diameter. Such a large enough domain precisely captures the flow bifurcations from the downstream dispersion. Moreover, an inside cylinder, representing the rotational domain, of a height of 0.04D and a radius of 0.17D was designed to simulate the flow around the rotating blades which contain the fluid immediately adjacent to the rotor.

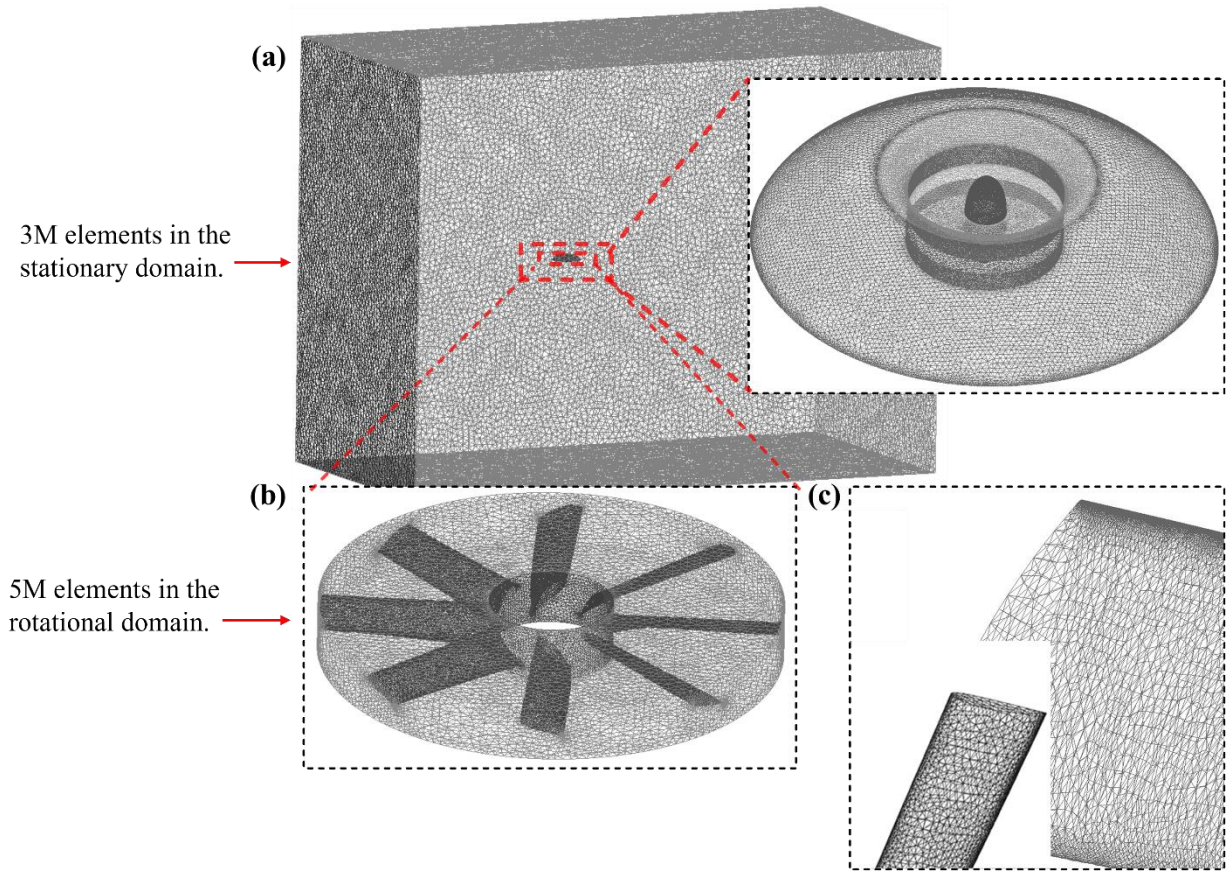


Figure 5: Mesh details. (a) UAV parts in the stationary domain, (b) in the rotational domain, and (c) zoom-in view of fine mesh on the rotor blades.

ANSYS ICEM CFD was applied as the tool for discretizing the control volume of the UAV generating the computational mesh. An unstructured mesh has been fabricated due to its robustness in analyzing the flow behavior around the aircraft [25]. Followed by the surface mesh as presented in Figure 5, with triangular elements by the method of path independency, a volume mesh was contrived inside the domains by the method of quick Delaunay [26] due to its versatility in tackling complex geometric domains. Figure 6 portrays the slice cut of the fine mesh boundary layer with the volumes. The meshes on the rotating fluid domain were progressively taken of smaller sizes close to the rotor surface. The smoothened volume mesh was next layered with 30 prismatic boundary layers on the UAV body parts. The discretization of the boundary layer mesh (prism layers) was generated with an expansion ratio of 1.2 and a first cell height within the range of $1.7 \times 10^{-5} - 4.3 \times 10^{-6}$mm corresponding to the non-dimensional $y^+ = 0.7$ and the increasing cruise speed. This is done to get more calculations per unit distance surrounding the near-wall region of the UAV because one intuitive way to achieve high-accuracy computational results is to place as many grid points as possible close to the wall so as to capture the velocity profile accurately and resolve the wake region of interest.

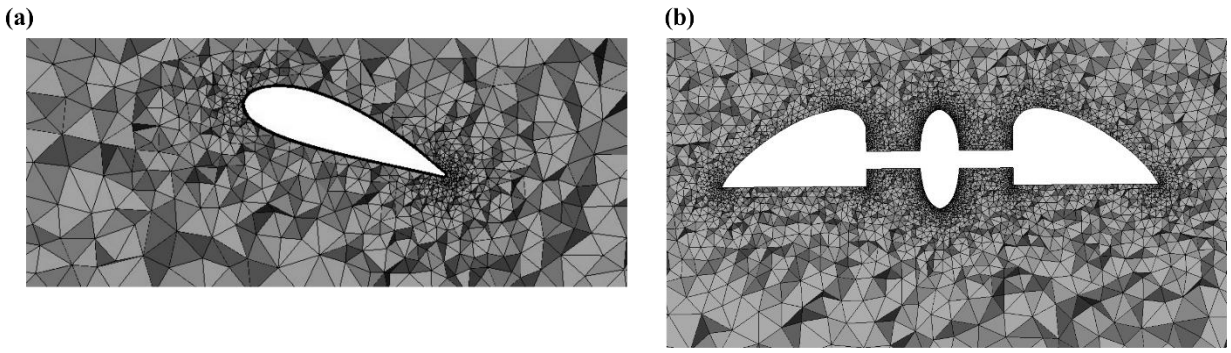


Figure 6: (a) Mid-section of the rotor showing the prism elements of the rotational domain and (b) volume mesh cut plane in the fluid density zone.

During the forward flight, as the airspeed increases with increasing flow Reynolds number, the boundary layer thickness is reduced referred to as the increasing freestream velocity requiring a high grid resolution close to the walls. Hence, a $y^+ < 1$ was achieved to dominate the flow separation and induce attached flow on the surface of the UAV. The attached flow profoundly minimizes the aerodynamic drag and enhances the efficiency of the vehicle.

*3.4 Physical Modeling and Boundary Conditions*

Fluid dynamics features are mostly studied in three primary directions: experiments, mathematical descriptions, and computational simulations. Compared to computational simulations, experiments are expensive, lengthy, and sometimes impossible to execute. In this study, high-fidelity computational fluid dynamics (CFD) simulations of the disc-shaped UAV were performed by a quasi-steady approach for the nonuniform flows in forward flight. The time-averaged form of the governing equations known as the three-dimensional Reynolds Averaged Navier Stokes Equations (RANS) was described by the solver in the form of an implicit algorithm. Although several techniques have been developed for aerodynamic simulations, till today the RANS model is the most widespread method for industrial applications [22]. The RANS governing equations use the Boussinesq (1877) eddy viscosity assumption to relate Reynold's stress tensor to the mean strain tensor. Simulation of the RANS equation greatly reduces the computational effort compared to a direct numerical simulation and is generally adopted for practical engineering calculations. However, the RANS equations require a turbulence model to approximate the real-world flow phenomena. The widely used [27], [28], [29] Menter's shear stress transport *SST k-ω* [30] turbulence model was selected in this study. The *SST k-ω* model predicts correctly the boundary layer separation which has been missed by the *k-ε* model. Furthermore, the *SST k-ω* turbulence model is advantageous such that the *k-ω* model is used in the inner region of the boundary layer and switches to the *k-ε* model in the free shear flow based on the grid density. Due to the application of a blending function ensuring a smooth transition between the two models, a NASA technical Memorandum rated the SST as the most accurate model for aerodynamic applications. In order to capture the laminar and turbulent boundary layers correctly, a high-resolution discretization scheme, known as the bounded second order upwind biased discretization, was applied in the RANS region for solving the mean flow, turbulence, and transition equations. The CFD

simulations were performed considering multiple reference frame (MRF) [22] due to its simplicity, fastness, and fair accuracy avoiding the prohibitively high computational effort required in the sliding mesh approach. The MRF rotational methodology allows the analysis of situations involving domains that are rotating relative to one another. For CFX, the MRF connects the relatively rotating domains by the "frozen rotor" [31] frame change of the interface model, 'general connection'. A frozen rotor method as well as an actuator disc approach, where the attitude of the rotating blades is relative to the rotor and is almost unchanged, significantly reduces the computational cost providing a valuable tool to investigate the lifting body aerodynamics. The specified pitch angles have a fixed orientation of $360^{o}$ across the interface. The far-field was treated as an opening boundary condition because it allows the fluid to cross the boundary surface in either direction of the domain. During the forward flight simulations, a velocity inlet and a pressure outlet were imposed. The velocity inlet ranged with subsonic speeds of 25-100 km/h and the corresponding incompressible flow Mach number varied in the range of 0.02-0.08 with a low turbulence intensity of 1%. The UAV body surfaces were considered no-slip boundary walls to avoid frictional drag. The ANSYS CFX Solver controlled the iterations by a physical timescale referring from the equation $0.1/\omega$ where $\omega$ stands for the rotational speed of the rotor. The physical timescale provides sufficient relaxation of the RANS equation non-linearities so that a converged steady-state solution is obtained. In actual multirotor configurations, because the RPM of each rotor continuously fluctuates even in the hovering state, an ideal steady phase is unrealistic to occur. However, in this study our octa-bladed rotor design dominates the unsteady fluctuations. Besides, the steady state approach, as employed in previous works of C. Paz et al. [31], compensates for the computational resources' limitations with logical viability. Throughout the simulations, air was treated as an ideal gas with constant density and specific heat at a static temperature of 288K relative to the heat transfer model, total energy. The total energy models the transport of enthalpy and includes the kinetic energy effects. All the simulations were performed with double precision and the determined convergence criteria of $10^{-4}$ for each residual. In context of the simulations, Table 2 presents the parameters of the calculated flight conditions.

Table 2: Calculated flight conditions.

| Forward speed (km/h) \ Tilt angle | $0^{o}$ | $4^{o}$ | $8^{o}$ | $12^{o}$ | Unit |
|---|---|---|---|---|---|
| 25 | 2840 | 2272 | 2090 | 1964 | rpm |
| 50 | 2730 | 2184 | 2009 | 1888 | |
| 75 | 2186 | 1748 | 1730 | 1626 | |
| 100 | 1276 | 750 | 720 | 700 | |

## 4. Results

*4.1 Mesh sensitivity analysis*

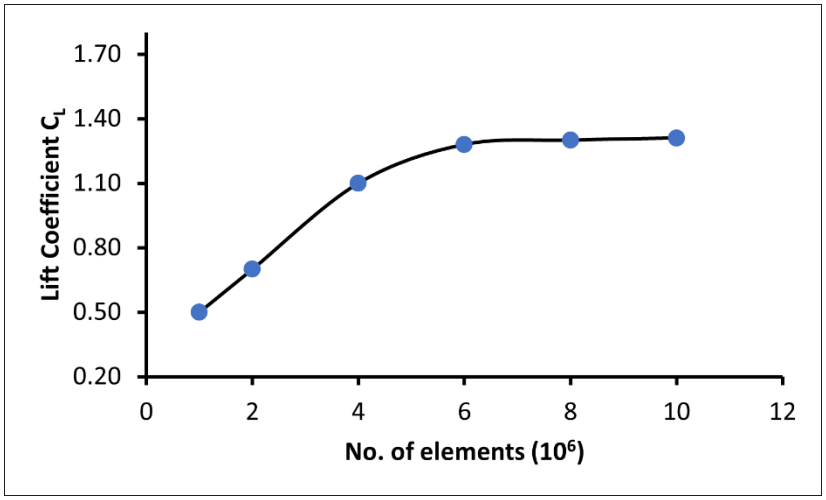


Figure 7: Mesh sensitivity analysis expressing the convergence of forward flight lift coefficient with the increasing number of grid elements.

A mesh sensitivity study tends to prescribe firm credence to the CFD simulation results. Accordingly, a mesh sensitivity analysis was conducted, consisting of running the same simulations with different grid resolutions. Six different cases were considered from 1M cells to 10M cells. During the forward flight, the lift coefficient, $C_L$ was treated as the criterion for the respective analysis. When the results were deemed to be mesh-independent the discrepancies with the preceding value were very minute ($< 1^{-3}$) as shown in Figure 7. Such a negligible variance was observed between simulation results for 8M and 10M grid elements. Thus, to reduce the computational resource limitations a topology of 8M cells, with 3M and 5M elements respectively on the stationary and the rotational domain, was applied throughout this study. The converged force coefficients during forward flight thus establish the validity of the computational model.

*4.2 Flow field analysis during forward flight at UAV level attitude*:

The pressure and velocity fields reveal clear aerodynamic trends with increasing forward speed. As shown in **Figure 8**, the low-pressure region over the curved upper surface expands with forward velocity, generating greater body lift. The rotor experiences a non-axisymmetric inflow in forward flight, producing an asymmetric pressure distribution. Increasing speed weakens the peak negative pressure on the upper surface and shifts the high-pressure region beneath the rotor rearwards, reducing the pressure gradient across the rotor and lowering thrust, while the enlarged rearward footprint corresponds to increased drag.

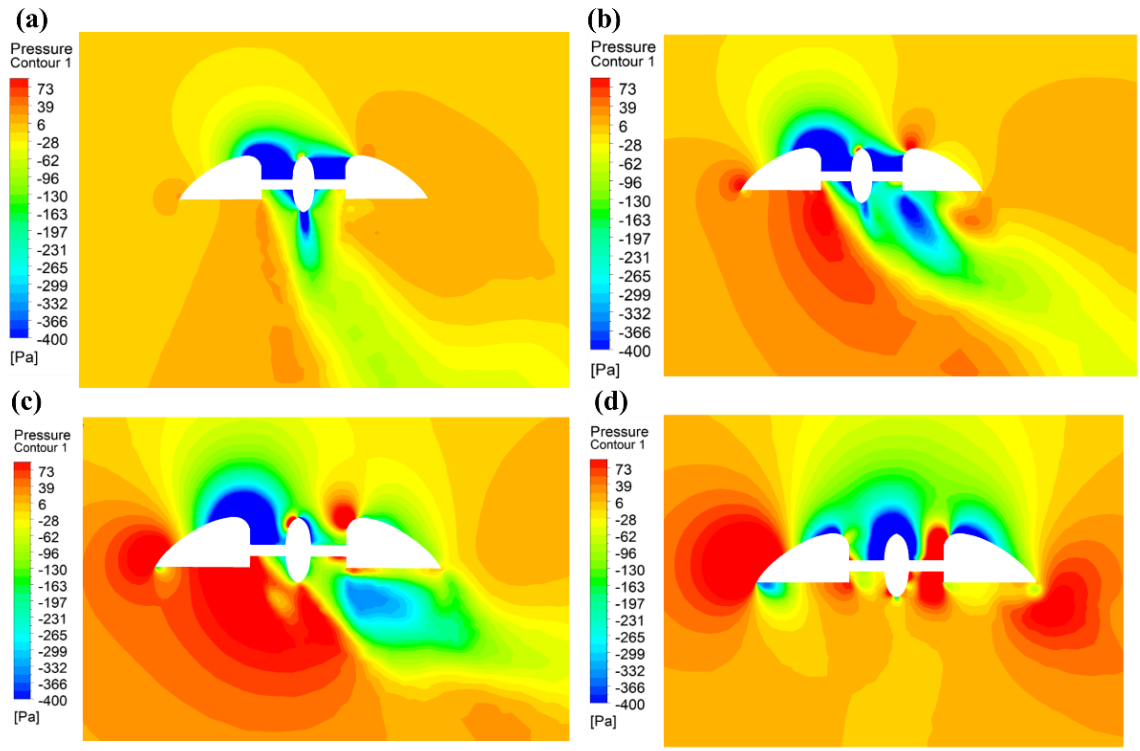


Figure 8: Pressure contour on the mid-plane XY, Z=0 (side view). (a) 25km/h, (b) 50km/h, (c) 75km/h, and (d) 100km/h. Fluid travels from the left towards the right of the cross-sectional plane denoting the left side as the advancing side of the UAV in forward flight with $0^{o}$ inclination (level attitude).

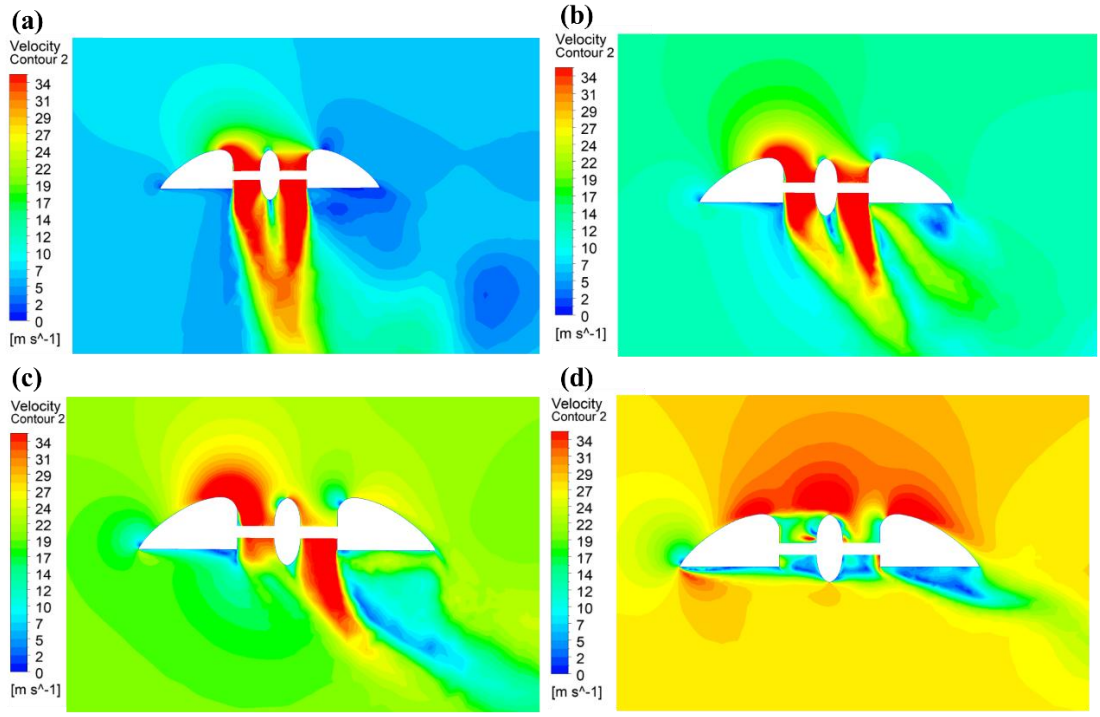

Figure 9: Velocity contour on the mid-plane XY, Z=0 (side view). (a) 25km/h, (b) 50km/h, (c) 75km/h, and (d) 100km/h. Fluid travels from left towards the right of the cross-sectional plane denoting the left side as the advancing side of the UAV in forward flight with 0° inclination (level attitude).

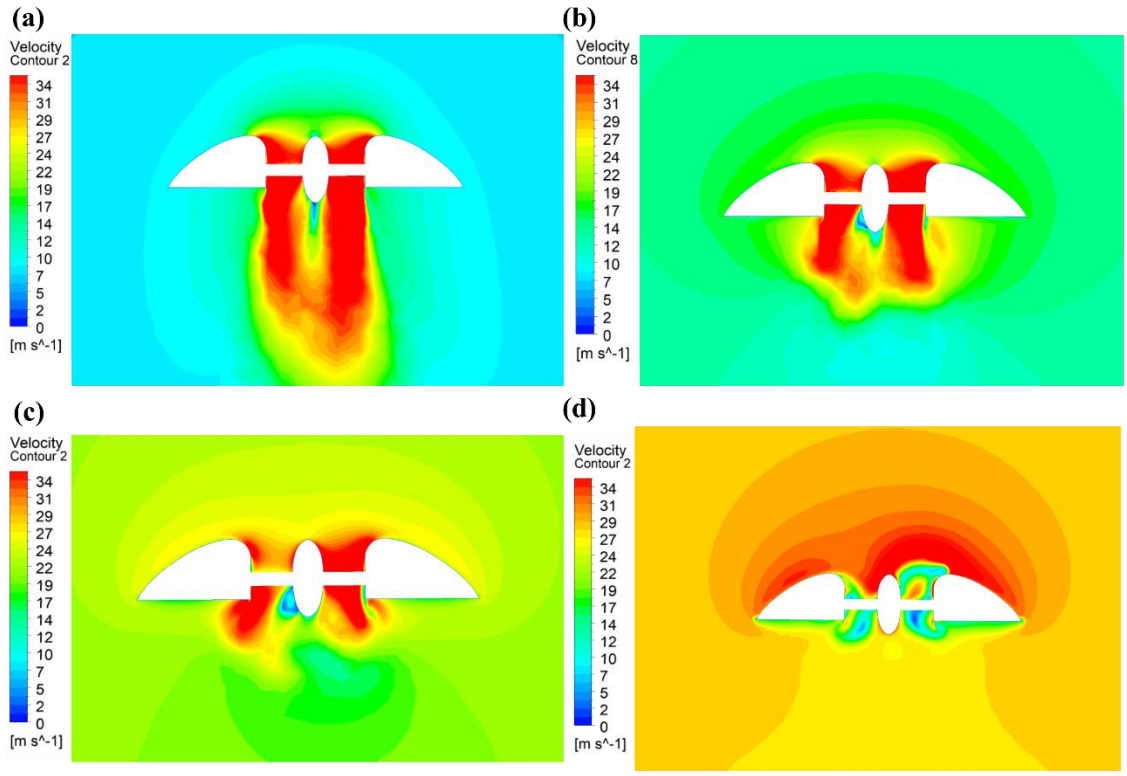


Figure 10: Velocity contour on the mid-plane ZX, Y=0 (front view) of the UAV with 0° inclination (level attitude). (a) 25km/h, (b) 50km/h, (c) 75km/h, and (d) 100km/h.

Velocity contours in **Figure 9** show that forward speed accelerates the flow over the upper curvature and progressively tilts the rotor wake downstream. Above 75 km/h, the wake aligns with the freestream, and rotor-induced downwash becomes significantly weaker, consistent with reduced rotor loading. The front-view velocity fields in **Figure 10** confirm that high-velocity downwash diminishes with increasing speed, indicating lower induced inflow and reduced power consumption.

Surface streamlines in **Figure 11** demonstrate that translational lift and body curvature streamline the flow during forward motion. At low speeds, high rotor RPM produces a strong vertical wake, whereas at higher speeds the wake decays rapidly and is swept downstream by the freestream. Velocity vectors in **Figure 12** show that the downwash tilts rearward with increasing speed, and the inflow through the rotor becomes more horizontal, reducing induced inflow and enhancing body-generated lift. At 100 km/h, a recirculating vortex forms behind the upper surface, contributing to increased pressure drag.

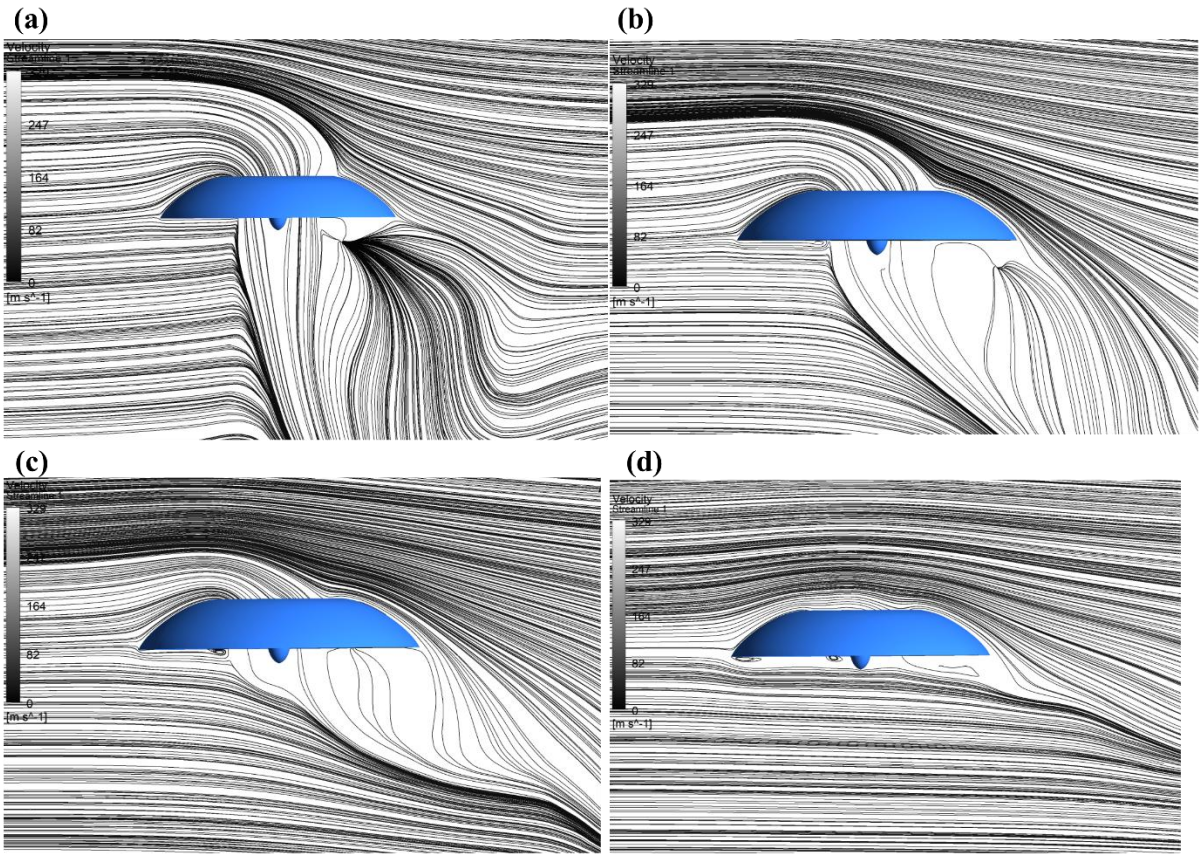


Figure 11: Surface streamlines on the mid-plane XY, Z=0 (side view) of the UAV with 0º inclination. (a) 25km/h, (b) 50km/h, (c) 75km/h, and (d) 100km/h.

Surface streamlines in **Figure 11** demonstrate that translational lift and body curvature streamline the flow during forward motion. At low speeds, high rotor RPM produces a strong vertical wake, whereas at higher speeds the wake decays rapidly and is swept downstream by the freestream. Velocity vectors in **Figure 12** show that the downwash tilts rearward with increasing speed, and the inflow through the rotor becomes more horizontal, reducing induced inflow and enhancing body-generated lift. At 100 km/h, a recirculating vortex forms behind the upper surface, contributing to increased pressure drag.

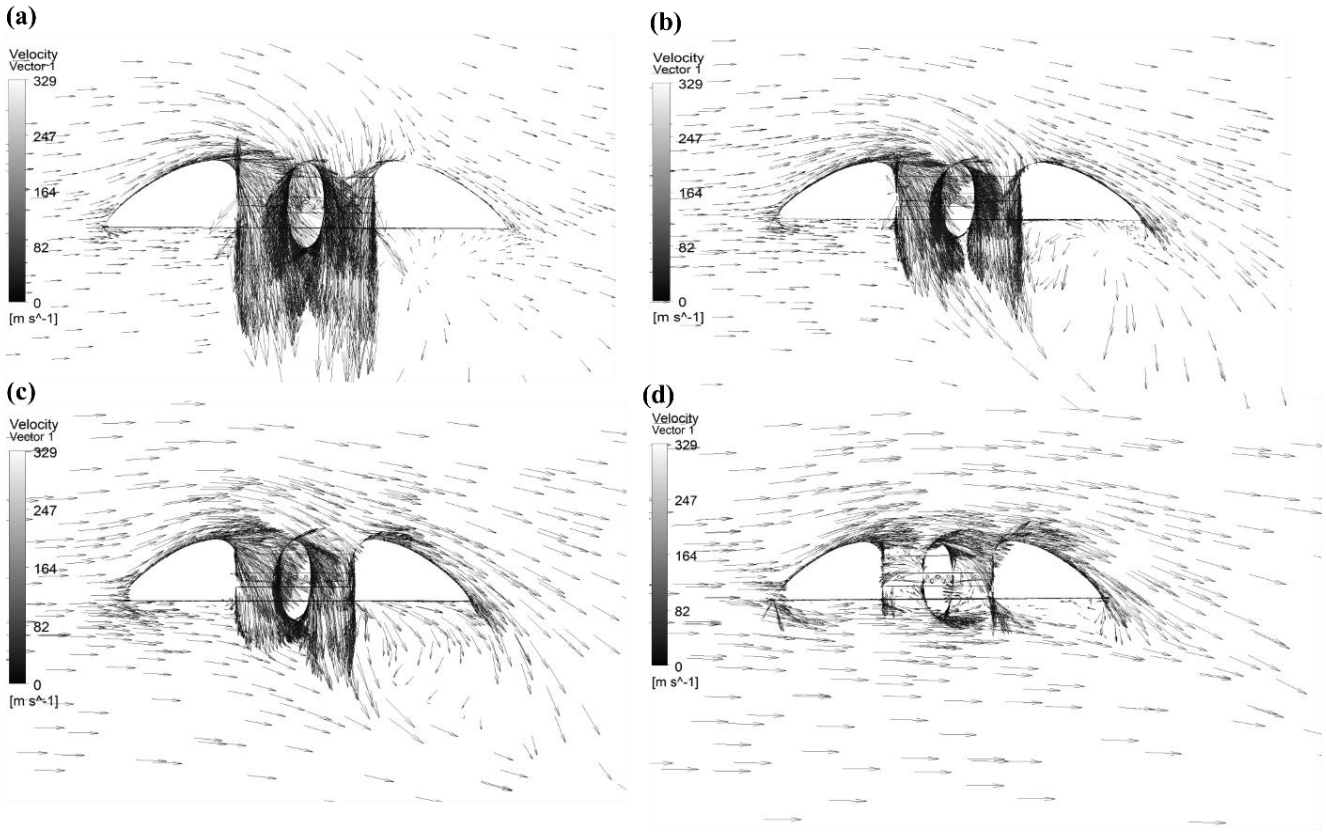


Figure 12: Velocity vector on the mid-plane XY, Z=0 (side view) of the UAV with 0º inclination. (a) 25km/h, (b) 50km/h, (c) 75km/h, and (d) 100km/h.

Overall, these results show that forward speed shifts lift generation from the rotor to the body, reduces induced inflow, and aligns the wake with the freestream that are the key mechanisms enabling improved aerodynamic efficiency in forward flight.

*4.3 Lift and Drag Assessment*

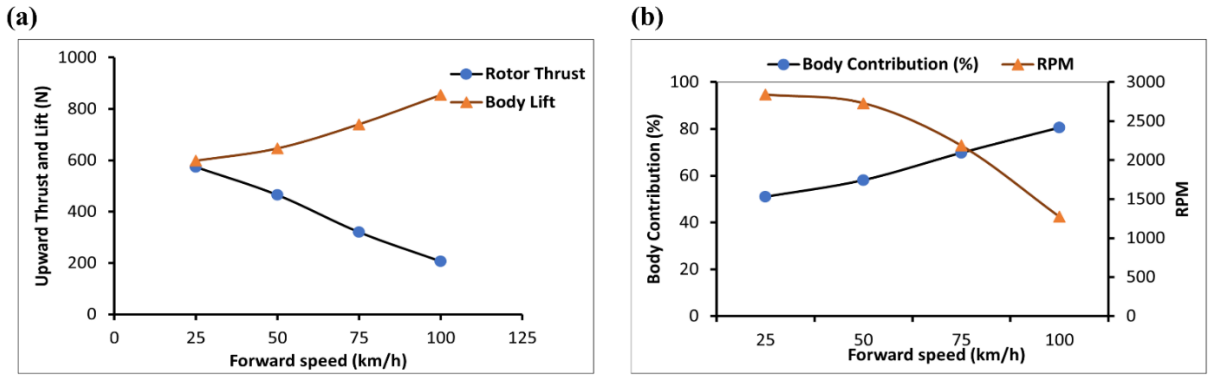


Figure 13: UAV lift at different forward speeds with 0º inclination to the flight path. (a) Rotor thrust and body lift at increasing forward speeds, (b) body lift percentage and the corresponding reduced RPM with the increasing forward speed during the level flight.

Once the UAV begins to accelerate to the forward steady level flight, the four aerodynamic forces: lift, weight, thrust, and drag are controlled by the use of the rotor RPM adjustment. As the forward airspeed increases, the rotor speed decelerates in order to maintain the same altitude. Moreover, the UAV upper body surface serves the purpose of a wing to the vehicle by enhancing its contribution to total lift generation in forward flight. Under most flying conditions, the impact of high pressure and the deflection of air from the lower surface of the UAV provides a small percentage of the total lift. The majority portion of lift is generated from the decreased pressure on the upper surface due to its curvature lip resembling an asymmetrical airfoil, rather than the increased pressure on the lower surface. Figure 13 indicates an increasing lift curve with respect to the rising forward speeds. The airflow speed on the cambered upper surface of the UAV increases and causes low pressure to generate lift. Correspondingly, the increasing lift contribution from the body significantly reduces the thrust requirement from the rotor to maintain the weight of the UAV while maneuvering in forward flight. A substantial contribution of 80.5% of the lift is generated from the UAV body surfaces during the maximum forward speed of 100km/h, while the rotor RPM is reduced to 1276. As a result, a rotor thrust of 0.19 of the UAV weight is sufficient to continue maneuvering at the maximum forward speed of 100 km/h. Rotor RPM is adjusted to keep the total lift constant while maintaining the equilibrium state of the straight and level flight. This considerable lift generation from the UAV body surfaces coherent to reduced RPM during the forward flight suggests an enhancement of the flight time in a power-efficient manner. However, the increase in lift links an increase in drag while transitioning from hover to high-speed forward flight. The drag and weight of the UAV considerably affect the flight time. The lesser the drag the more the flight time of the vehicle. The drag is interlinked to geometrical and physical parameters such as the UAV body shape, wing-like upper surface curvature, and flight speed. In the later section, drag improvement is approached by tilting the UAV to the wind.

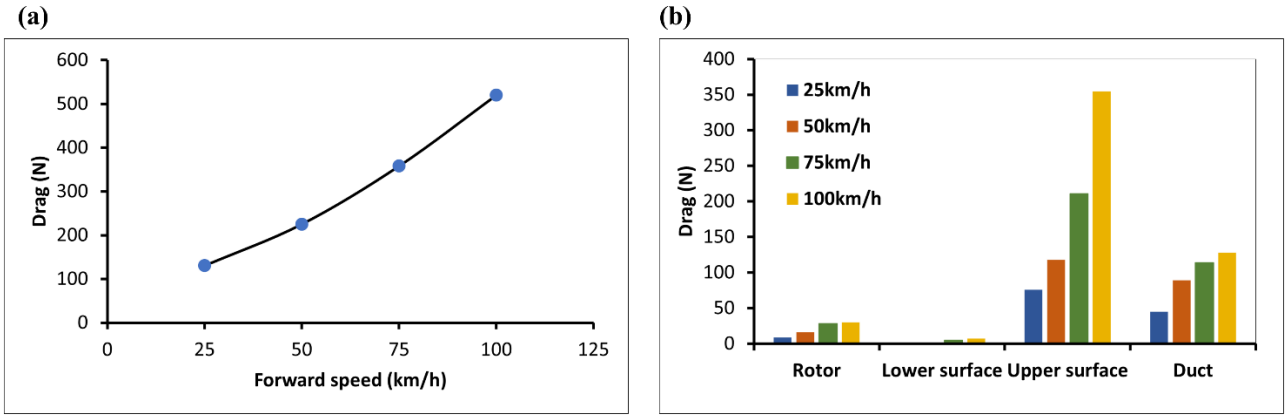


Figure 14: (a) UAV Drag at increasing forward speeds, and (b) drag distribution during the forward level flight with 0° inclination to the wind.

Drag acts in the streamwise direction rearward to the UAV motion as a resistance while passing through the air, caused by friction and difference in air pressure. Physically, with the increasing forward speed, the pressure differential on the upper and lower surface of the UAV body decreases which results in the generation of augmented drag. The bottom streamlines remain minimally

disturbed and continues parallel to the fluid flow, which supports the negligible drag generated from the lower surface as presented in Figure 14. However, the upper surface generates more drag with the increasing forward speed due to the downwash caused by the trailing edge vortices. With the increase of forward speed, the disruption of airflow by the UAV body surfaces and rotor disc is occurring at greater force which in return increases the retarding force or the drag acting relative to the wind and opposite to the flight path. Thus, the physical drag is increasing as a factor of the square of the forward speed.

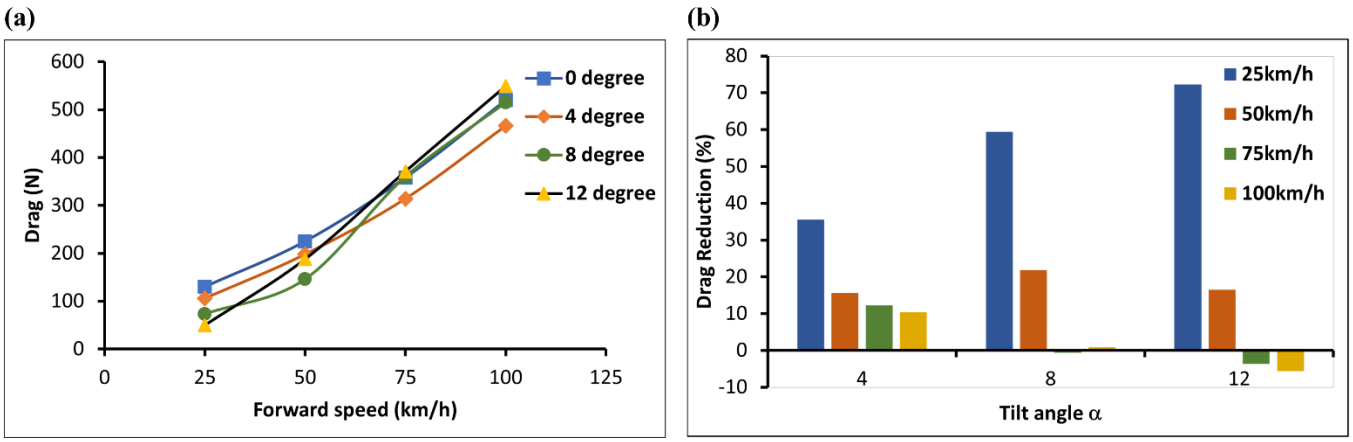


Figure 15: (a) Increasing drag with respect to forward speeds at different attitudes of the UAV in forward flight and (b) Percentage of drag reduction at different tilt angles compared to level attitude of the UAV during forward flight. A higher percentage of drag reduction with a maximum of 72% is achieved while the UAV flies at 25km/h with a 12° tilt towards the flight path. As the tilt angle increases, the aerodynamic efficiency of the UAV increases with reduced drag to overcome.

In order to approach the drag improvement and enhance the rotor power efficiency, the UAV is tilted towards the flight path having a forward force of thrust inducing a negative angle of attack ($AOA < 0$). Thus, the rotor disc plane is leaning with a horizontal component generating a forward thrust to overcome the drag and a vertical component contributing to the lift in order to balance the weight of the UAV during forward flight. The corresponding rotor RPM is reduced, as presented in Table 2, because the UAV in the inclined flight attitude generates low drag and contributes to the aerodynamic lift even for a small negative angle of attack. Figure 15 illustrates that the drag increases greatly with the increase of forward speed, however, is reduced significantly by 72% during the forward speed of 25km/h with 12° inclination of the UAV towards the oncoming air. This significant reduction with respect to the tilt angle is due to the fact that the lifting surface of the duct and the upper body lip curvature favors the flow being greatly streamlined, supported by Figure 16, with minimal pressure drag rearwards maintaining attached flow on the UAV's trailing edge. During low-speed flight with forward inclinations, a large improvement in drag characteristics is achieved through the reduction of adverse pressure gradients by lowering the negative pressure peak at the UAV lower surface. However, with the increase in forward speed, the percentage of drag reduction decreases denoting a decrease in the optimum inclined angle. In comparison, during 100km/h as the tilt angle of the UAV increases beyond 4°, the advancing side

of the lower surface results in the induction of a substantial download and a higher drag growth rate generated from weaker pressure difference. High-speed flights with larger inclinations generate more drag because due to the reduced RPM, part of the flow is spilled out of the rotor disc above the upper surface producing vortices with a deflection of the wake from the rotation axis. This is supported by the fact that during low-speed flight, lifting airfoils demonstrate minimum drag with larger angles of attack while the converse is true for high-speed flights. Following the airfoil theory, during the forward speed of 50km/h the minimum drag is achieved at a lesser inclination of 8º which further decreases to 4º as the flight speed goes beyond 50km/h. Accordingly, the maximum drag reduction of 10.5% is achieved during the high-speed forward flight of 100km/h with a small inclination of 4º towards the oncoming air. Lower air speeds have a greater percentage of drag reduction because the rotor blades' angle of attack is usually higher at lower air speeds. So, the drag generated from the rotor is considerably low. The flow of air through the rotor disc is more horizontal, which reduces induced inflow and drag with a corresponding angle of attack. Moreover, with respect to the optimum tilt angle at every forward speed, the work done by the rotor to lift the UAV into the air and to generate forward force opposing the drag is reduced as seen by the low-velocity gradient in the region neighboring the rotor disc (Figure 17). Thus, the required thrust is reduced by the inclination approach in forward flight. This augments the efficiency of the UAV with each forward speed gained by horizontal movement of the UAV.

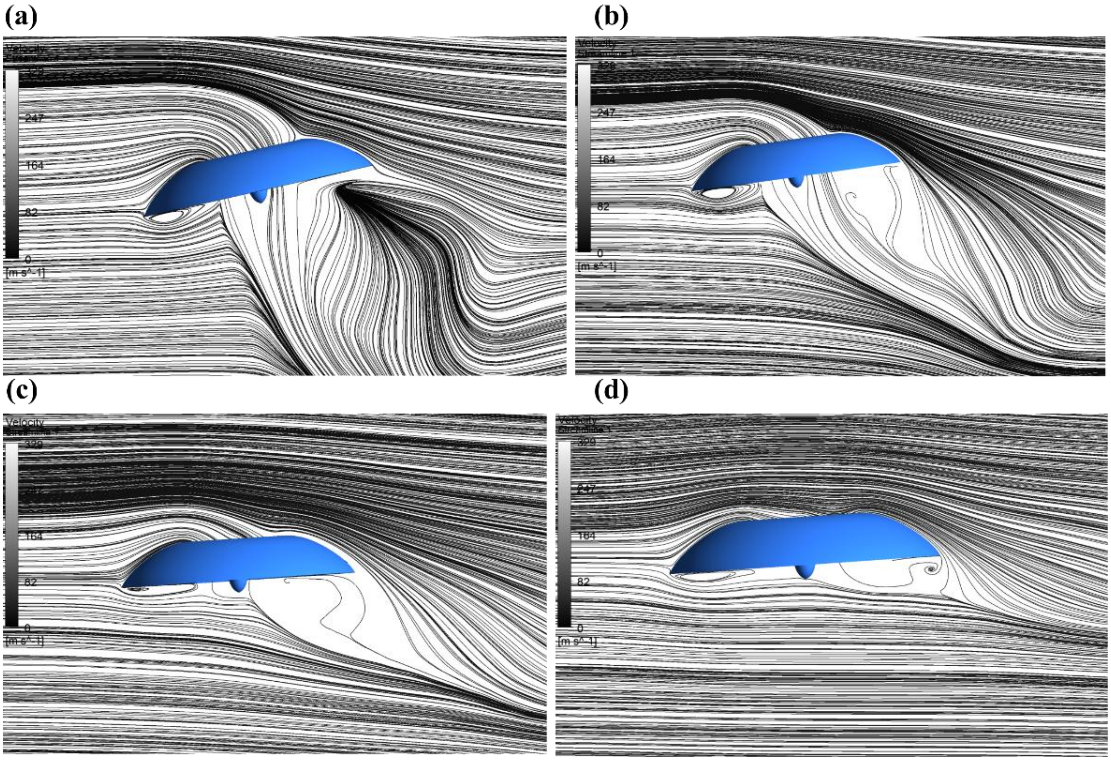


Figure 16: Surface streamlines through the mid-plane XY, Z=0 (side view) at optimum inclined angles of (a) 12º at 25km/h, (b) 8º at 50km/h, (c) 4º at 75km/h, and (d) 4º at 100km/h.

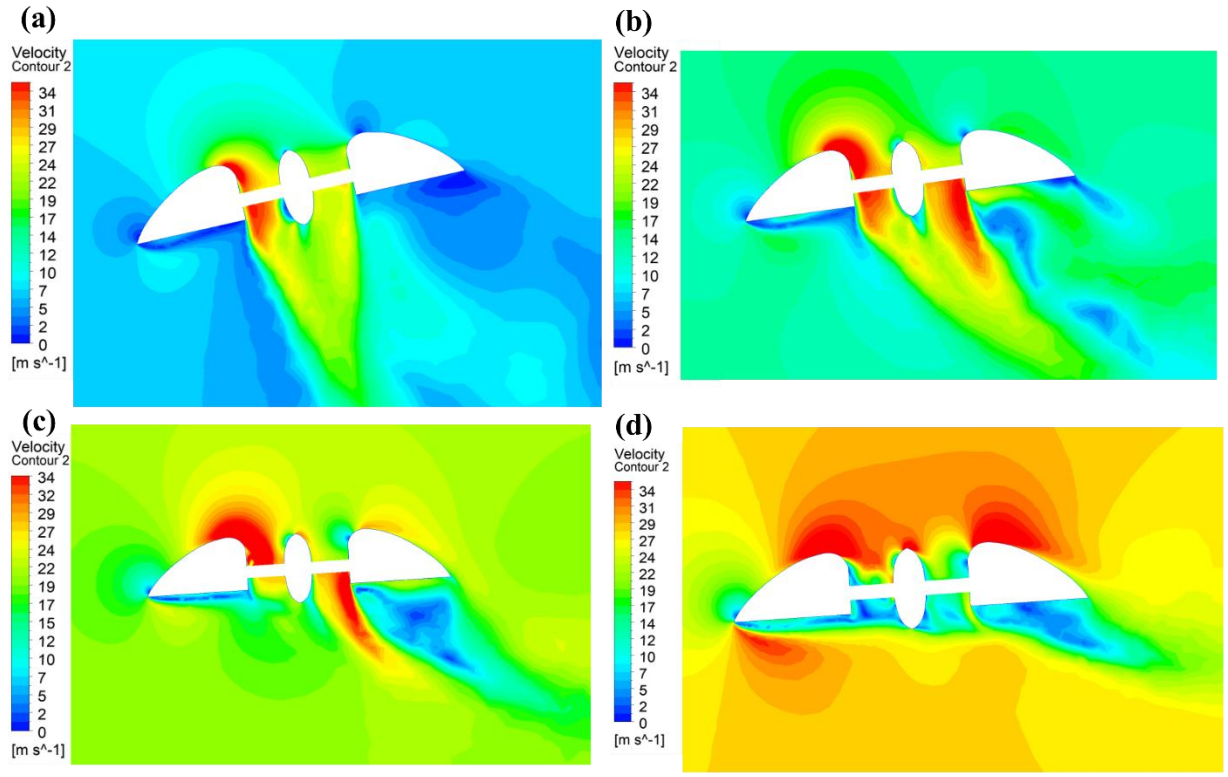


Figure 17: Velocity contour through the mid-plane XY, Z=0 (side view) at optimum inclined angles of (a) 12° at 25km/h, (b) 8° at 50km/h, (c) 4° at 75km/h, and (d) 4° at 100km/h.

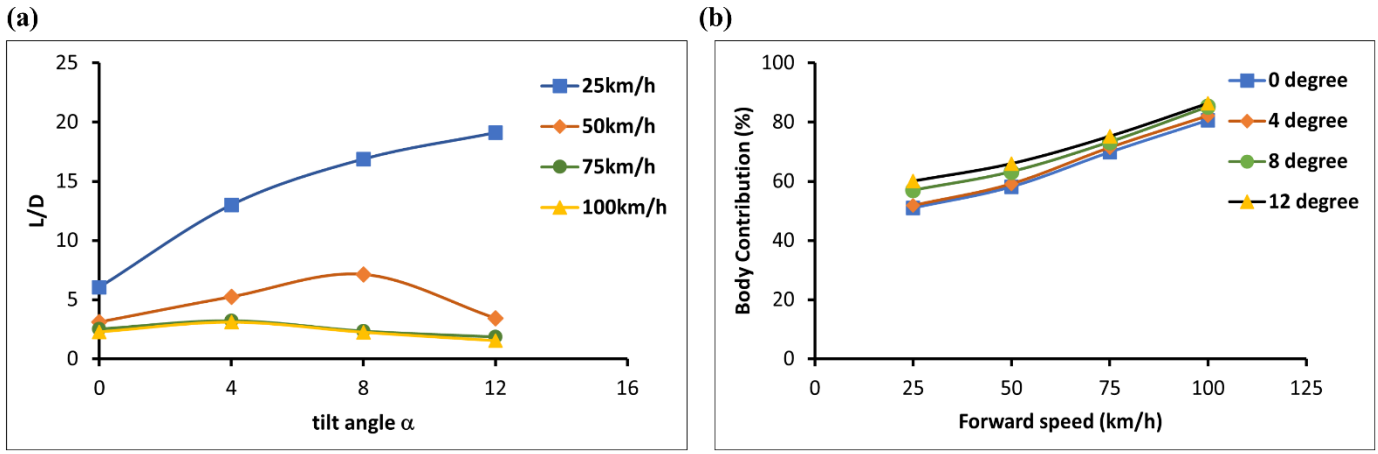


Figure 18: (a) Lift-to-Drag ratio (L/D) with respect to different inclinations during the forward flights ranging from low to high velocities and (b) corresponding body lift percentage with increasing forward speeds at different tilt angles.

The minimum drags due to the fact that the flow on the UAV's upper surface is greatly entrained to the lifting rotor system at different tilt angles is associated with the maximum lift-to-drag (L/D) ratio during the equilibrium state of straight and level flight, where lift varies slowly in order to

maintain the UAV weight. Figure 18 indicates that the higher the forward speed, the lower the tilt angles generating the maximum lift-to-drag. A maximum L/D of 19.09 is achieved during the forward speed of 25km/h with a 12° tilt angle towards the wind. Lift continues to be shared by the body lift owing to the phenomena that as the forward speed increases, the area of low pressure at the leading edge of the upper surface also increases resulting in a gradual increase in the positive lift contribution from the body. This accounts for the fact that the greater the tilt angle the less the disturbing effect of the rotor wake on the UAV upper surface. With small inclinations, the UAV's body surfaces generate a greater portion of lift of a maximum of 86.4% during the forward speed of 100km/h at 12° tilt towards the wind. However, as the forward speed increases, a larger tilt angle shows a greater drag from the trailing edge vortices of air encountering more area of the UAV. As a result, the higher the forward speed, the less the tilt angle generating the optimum L/D. Noteworthily, forward inclinations of the UAV towards the flight path result in a negative angle of attack which reduces the total lift slightly, however, have some forward thrust to compromise. The total lift is sustained by the rotor RPM adjustment. Additionally, tilting the UAV into the wind reduces the angle of attack of rotor blades thus reducing their capacity to generate thrust. The faster the UAV travels with the increasing forward speed, the less thrust is available from the rotors, so there is a speed limit from this effect as well as from the drag through the air.

*4.4 Thrust and Power Assessment*

As forward speed increases, the incoming flow reduces the induced velocity required through the rotor, causing rotor thrust to drop while the disc-shaped body supplies a growing share of lift through enhanced low-pressure regions on the upper surface. Small negative tilt angles further reduce rotor loading by redirecting part of the thrust forward and improving flow attachment over the body. This combination lowers the thrust-to-weight ratio with speed and inclination, indicating higher aerodynamic efficiency. Figure 19 specifies that the higher forward speed with the inclinations of the UAV towards the flight path diminishes the thrust-to-weight ratio which consequently increases the power-saving percentage. This is supported by the fact that the body surfaces generate a substantial amount of lift force achieved by lower pressure peaks on the upper body lip curvature. Across all conditions, power savings range from **25.26%** to **80.26%**, confirming that body-generated lift and tilt-induced drag reduction significantly enhance forward-flight performance and endurance.

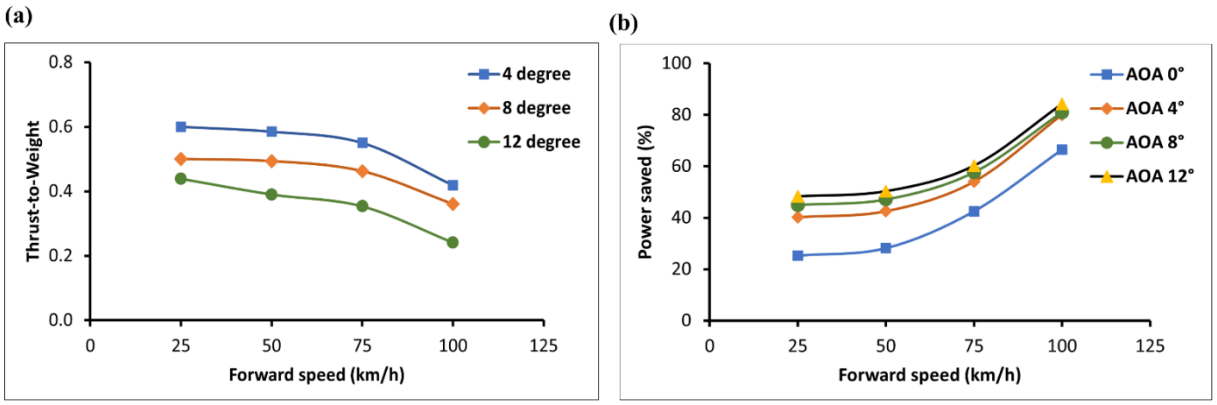

Figure 19: (a) Forward thrust-to-weight ratio at different flight speeds; adjusted by the control of the rotor RPM, and (b) percentage of power saved during forward flight with respect to hovering of the UAV.

*4.5 Optimum performance of the UAV in forward flight*.

Table 3 presents the optimum flight results of the UAV based on the design and simulation scenarios. Tilting the UAV into a small negative angle of attack reduces drag by improving flow entrainment over the disc-shaped body while maintaining the required lift through rotor RPM adjustment. Each forward speed exhibits a distinct inclination that minimizes drag and maximizes the lift-to-drag ratio. At **25 km/h**, the optimal tilt is **12°**, yielding the highest L/D and **48.31%** power savings. As speed increases, the optimal inclination decreases; beyond **50 km/h**, maximum efficiency occurs at **4°**. At **100 km/h**, a **4°** tilt provides the best performance, producing **0.418 W** forward thrust and **80.26%** power savings relative to hover.

Table 3: Optimum flight results of the UAV in forward flight.

| Flight speed (km/h) | Optimum inclined angle (°) | Maximum L/D | Thrust-to-Weight ratio | Power saved (%) |
|---|---|---|---|---|
| 25 | 12 | 19.09 | 0.43 | 48.31 |
| 50 | 8 | 7.14 | 0.49 | 50.3 |
| 75 | 4 | 3.22 | 0.55 | 54 |
| 100 | 4 | 3.09 | 0.418 | 80.26 |

These results demonstrate that initiating forward flight from a negative angle of attack is an effective drag-reduction strategy, enabling substantial power savings and extended flight range. The disc-shaped configuration benefits strongly from inclination-induced flow alignment, making it well-suited for long-distance, energy-efficient missions.

## 5. **Discussions**

Forward flight simulations of the disc-shaped UAV reveal significant aerodynamic changes compared to hover mode. Unlike axisymmetric rotor behavior in vertical flight, forward motion introduces periodic asymmetry in pressure and velocity distributions due to blade rotation relative to airflow. The upper surface of the UAV experiences reduced pressure with increasing axial flow, generating greater lift than the lower surface.

As forward speed increases, drag rises significantly, opposing motion. Rotor blades encounter combined rotational and translational airflow, resulting in higher velocities on the advancing side and lower on the retreating side. This asymmetry produces a central high-velocity wake that diffuses laterally, aligning with the flow direction at higher speeds.

Rotor wake behavior shifts with speed and RPM. At low speeds (25 km/h), strong downwash dominates below the UAV. As speed increases, wake tilts rearward and decays faster due to reduced rotor RPM. The disc-shaped body enhances entrained flow, minimizing wake disturbance and improving lift generation.

Transitioning from hover to forward flight reduces power demand due to favorable inflow angles and increased body lift. At 100 km/h, the UAV achieves up to 80.5% lift from its upper surface, allowing lower rotor RPM to sustain level flight.

Tilting the UAV introduces a negative angle of attack, reducing lift but enhancing forward thrust. The curved upper surface compensates by generating up to 86.4% of lift, maintaining altitude. Increased tilt also improves drag performance by reducing rotor RPM, which lowers rotor-induced drag. This strategy minimizes flow separation and turbulence, enhancing aerodynamic efficiency.

## 6. Conclusions

This study numerically evaluated the forward-flight aerodynamics of a disc-shaped high-lift UAV and demonstrated that its curved upper surface enables substantial lift generation and power savings across a wide speed range. The UAV's body provides up to **80.5%** of total lift at 100 km/h, reducing rotor thrust to **0.19 W** of the vehicle weight and yielding **66.42%** power savings in level flight. Tilting the UAV further enhances efficiency, with a maximum lift-to-drag ratio of **19.09** at 12° and 25 km/h, and peak power savings of **80.26%** at 100 km/h and 4°. These results highlight the aerodynamic advantages of the disc-shaped configuration, particularly its ability to shift lift generation from the rotor to the body, supporting its suitability for long-range, power-efficient missions in urban surveillance and atmospheric monitoring. The findings also provide a foundation for future optimization involving intelligent control strategies, payload-dependent aerodynamics, and experimental validation.

### Author Contributions

The idea of the current findings portrayed in this study was conceptualized and supervised by S.-H.C.; throughout the methodology, the simulations were conducted by S.S.A.S.; data analysis and writing the original draft were prepared by S.S.A.S. All authors have read and agreed to the submitted version of the manuscript.

### Funding Statement

This research did not receive any specific grant from funding agencies in the public, commercial, or not-for-profit sectors.

### Data Availability Statement

The data available in this study are available on request from the corresponding author.

### Declaration of Conflicting Interests

The authors declare that they have no known competing financial interests or personal relationships that could have appeared to influence the work reported in this paper.

### References

1. Nex, F., et al., *UAV in the advent of the twenties: Where we stand and what is next.* ISPRS Journal of Photogrammetry and Remote Sensing, 2022. **184**: p. 215-242.

2. Hassanalian, M. and A. Abdelkefi, *Classifications, applications, and design challenges of drones: A review.* Progress in Aerospace Sciences, 2017. **91**: p. 99-131.
3. Marino, M., et al., *An Evaluation of Multi-Rotor Unmanned Aircraft as Flying Wind Sensors.* International Journal of Micro Air Vehicles, 2015. **7**(3): p. 285-299.
4. Ahmed Snikdha, S.S. and S.-H. Chen, *A Computational Investigation of the Hover Mechanism of an Innovated Disc-Shaped VTOL UAV.* Drones, 2023. **7**(2): p. 105.
5. Rasuo, B. and N. Mirkov, *On the possibility of using Coanda Effect for Unmanned Aerial Vehicles – a numerical investigation.* PAMM, 2014. **14**.
6. Barlow, C., et al., *Investigating the use of the Coanda Effect to create novel unmanned aerial vehicles*, in *International Conference on Manufacturing and Engineering Systems*. 2009, 386-391: Huwei, Taiwan.
7. Theys, B. and J. Schutter, *Forward flight tests of a quadcopter unmanned aerial vehicle with various spherical body diameters.* International Journal of Micro Air Vehicles, 2020. **12**: p. 175682932092356.
8. Simic, M., C. Bil, and V. Vojisavljevic, *Investigation in wireless power transmission for UAV charging.* Procedia Computer Science, 2015. **60**: p. 1846-1855.
9. Xiao, K., et al., *A Lifting Wing Fixed on Multirotor UAVs for Long Flight Ranges*, in *2021 International Conference on Unmanned Aircraft Systems (ICUAS)*. 2021: Athens, Greece. p. 1605-1610.
10. Petrolo, M., et al., *On the development of the Anuloid, a disk-shaped VTOL aircraft for urban areas.* Advances in Aircraft and Spacecraft Science, 2014. **1**(3): p. 353-378.
11. Pham, K.L., et al., *The Study of Electrical Energy Power Supply System for UAVs Based on the Energy Storage Technology.* Aerospace, 2022. **9**(9): p. 500.
12. Yang, Y., et al., *Aerodynamic and Aeroacoustic Performance of an Isolated Multicopter Rotor During Forward Flight.* AIAA Journal, 2020. **58**(3): p. 1171-1181.
13. Yang, H., et al., *Multi-rotor drone tutorial: systems, mechanics, control and state estimation.* Intelligent Service Robotics, 2017. **10**: p. 79-93.
14. Lee, J.Y., et al. *Modeling and control of a saucer type Coandä effect UAV*. in *2017 IEEE International Conference on Robotics and Automation (ICRA)*. 2017. Singapore.
15. Davoudi, B. and K. Duraisamy. *A Hybrid Blade Element Momentum Model for Flight Simulation of Rotary Wing Unmanned Aerial Vehicles*. in *AIAA Aviation 2019 Forum*. 2019. Dallas, Texas.
16. Hwang, M.-h., H.-R. Cha, and S.Y. Jung, *Practical Endurance Estimation for Minimizing Energy Consumption of Multirotor Unmanned Aerial Vehicles.* Energies, 2018. **11**(9): p. 2221.
17. Stolaroff, J.K., et al., *Energy use and life cycle greenhouse gas emissions of drones for commercial package delivery.* Nature Communications, 2018. **9**(1): p. 409.
18. Vargas Loureiro, E., et al., *Evaluation of low fidelity and CFD methods for the aerodynamic performance of a small propeller.* Aerospace Science and Technology, 2021. **108**: p. 106402.
19. He, P., et al., *An aerodynamic design optimization framework using a discrete adjoint approach with OpenFOAM.* Computers & Fluids, 2018. **168**: p. 285-303.
20. Izadi, M.J. and A. Falahat. *Effect of blade angle of attack and hub to tip ratio on mass flow rate in an axial fan at a fixed rotational speed*. in *Fluids Engineering Division Summer Meeting*. 2008.
21. Kelly, N.Q., Z. Siddiqi, and J.W. Lee, *Computational fluid dynamics analysis and optimization of the Coanda unmanned aerial vehicle platform.* International Journal of Mechanical and Mechatronics Engineering, 2020. **14**(12): p. 592-597.
22. Liu, X., D. Zhao, and N.L. Oo, *Comparison studies on aerodynamic performances of a rotating propeller for small-size UAVs.* Aerospace Science and Technology, 2023: p. 108148.
23. Li, Y., et al., *A biomimetic rotor-configuration design for optimal aerodynamic performance in quadrotor drone.* Journal of Bionic Engineering, 2021. **18**(4): p. 824-839.

24. Galway, D., J. Etele, and G. Fusina, *Modeling of urban wind field effects on unmanned rotorcraft flight.* Journal of aircraft, 2011. **48**(5): p. 1613-1620.
25. Kyrkos, A. and J.A. Ekaterinaris, *Assessment of an unstructured mesh approach for CFD predictions of the NH90 fuselage rotor.* Aerospace Science and Technology, 2012. **19**(1): p. 77-85.
26. Tomac, M. and D. Eller, *From geometry to CFD grids—An automated approach for conceptual design.* Progress in Aerospace Sciences, 2011. **47**(8): p. 589-596.
27. Lei, Y., Y. Li, and J. Wang, *Aerodynamic Analysis of an Orthogonal Octorotor UAV Considering Horizontal Wind Disturbance.* Aerospace, 2023. **10**(6): p. 525.
28. Steijl, R., G. Barakos, and K. Badcock, *A framework for CFD analysis of helicopter rotors in hover and forward flight.* International journal for numerical methods in fluids, 2006. **51**(8): p. 819-847.
29. Barakos, G.N., et al., *CFD simulation of helicopter rotor flow based on unsteady actuator disk model.* Chinese Journal of Aeronautics, 2020. **33**(9): p. 2313-2328.
30. Menter, F.R., *Two-equation eddy-viscosity turbulence models for engineering applications.* AIAA Journal, 1994. **32**(8): p. 1598-1605.
31. Paz, C., et al., *Assessment of the methodology for the CFD simulation of the flight of a quadcopter UAV.* Journal of Wind Engineering and Industrial Aerodynamics, 2021. **218**: p. 104776.